

Time-lapse poroelastic modelling for a carbon capture and storage (CCS) project in Alberta

Shahin Moradi, Don C. Lawton, and Edward S. Krebs

ABSTRACT

A finite-difference algorithm was developed based on the Biot's equations of motion for modelling wave propagation in poroelastic media. In contrast with the elastic modelling, in the poroelastic approach the properties of the pore fluid are taken into account in the algorithm. Poroelastic modelling could be useful in cases where the fluid content of the rock is of interest, i.e. Carbon Capture and Storage (CCS) projects. We examined our program using a model based on the Quest CCS project in Alberta to investigate the detectability of CO_2 after one year of injection. This was done by defining two models for baseline and monitor scenarios that represented the subsurface before and after injecting CO_2 . The difference between the calculated seismic sections for the two scenarios shows that the residual amplitude is comparable with the signal amplitude. With this result, the injected CO_2 in the Quest project over a year could be detected providing the data have good bandwidth and a high signal-to-noise ratio. The effect of the porosity and the fluid properties on the output of the algorithm is being examined in an ongoing study.

INTRODUCTION

Wave propagation in porous media has attracted attention in the last fifty years since Maurice Biot established his theory on poroelasticity (Biot, 1962). Biot's theory could be used in the oil and gas industry for exploration and monitoring purposes. It could also be used for the detection of CO_2 in Carbon Capture and Storage (CCS) projects where CO_2 is injected into deep geological formations for permanent storage. A poroelastic medium is composed of two phases. One phase is the porous elastic solid frame, and the other is the compressible viscous pore fluid that can move within the pore space. The relative movement of the fluid with respect to the solid generates a "slow P-wave" that travels with a velocity close to the wave velocity in the fluid. The wave-induced fluid flow leads to energy dissipation in the medium that is often neglected in elastic modelling algorithms. Some studies show that the presence of the slow P-wave in the fluid saturated media may change the seismic wave-field noticeably (Gurevich et al., 1997; Shapiro and Müller, 1999). At seismic frequencies the viscosity effects become stronger than the internal effects. Thus, the slow p-wave diffuses when traveling through the medium. However, if the viscosity is zero, the slow P-wave is a travelling wave at all ranges of frequency (Carcione et al., 2010).

There have been extensive numerical examination studies of Biot's theory since the fluid content of the rock is always of interest in reservoir characterization and monitoring. Carcione et al. (2010) presented a comprehensive review on the numerical methods used for poroelastic media. Sheen et al. (2006) used a staggered-grid velocity-stress finite-difference for a gas-water interface and Dai et al. (1995) employed a MacCormack finite-difference scheme for simulating the wave motion in poroelastic media.

Having an effective boundary condition is essential in any finite-difference wave mod-

elling algorithm to avoid artificial reflections from the computational boundaries. The perfectly matched layer (PML) was introduced by Berenger (1994) for electromagnetic waves and was later used by Chew and Liu (1996) for elastic waves. This layer is defined so that the reflection coefficient at the computational boundary is zero at all angles and the outgoing waves are absorbed as much as possible. In this work this boundary condition is used for a poroelastic finite-difference algorithm that was previously developed by the authors (Moradi and Lawton, 2013). The modelling algorithm is based on the Biot's theory of poroelasticity (Biot, 1962) and the medium is assumed to be porous and saturated with fluid. The finite-difference scheme that we use is similar to that of Sheen et al. (2006). However, our numerical examples are from a CO_2 storage project, and we would like to examine the algorithm for possible monitoring purposes in these type of projects. Therefore, we present a poroelastic time-lapse modelling study later in this report.

THEORY

Biot's theory of poroelasticity

Maurice Biot (1962) was the first to establish the theory of poroelasticity. He made the following assumptions to derive the equations of motion in the porous media: (1) the rock frame is assumed to be elastic and isotropic; (2) the pores are connected so that the fluid could travel through the pore space; (3) the seismic wavelength is much larger than the average pore size; and (4) the deformations are small enough that the mechanical processes become linear. Although Biot extended his theory to other cases such as anisotropic media, in this work we focus on the isotropic case. The partial differential equations for the isotropic poroelastic media could be written as first order equations in time:

$$\frac{\partial \tau_{ij}}{\partial t} = 2\mu \frac{\partial e_{ij}}{\partial t} + \left(\lambda_c \frac{\partial e_{kk}}{\partial t} + \alpha M \frac{\partial \varepsilon_{kk}}{\partial t} \right) \delta_{ij} \quad (1)$$

$$\frac{\partial P}{\partial t} = -\alpha M \frac{\partial e_{kk}}{\partial t} - M \frac{\partial \varepsilon_{kk}}{\partial t} \quad (2)$$

$$\frac{\partial W_i}{\partial t} = A \frac{\partial \tau_{ij}}{\partial x_j} + B \frac{\partial S}{\partial x_i} + C W_i \quad (3)$$

$$\frac{\partial V_i}{\partial t} = D \frac{\partial \tau_{ij}}{\partial x_j} + E \frac{\partial S}{\partial x_i} + F W_i \quad (4)$$

where $e_{ij} = \frac{1}{2} \left(\frac{\partial u_i}{\partial x_j} + \frac{\partial u_j}{\partial x_i} \right)$ is the solid strain, with u being the particle displacement of the solid, and $\varepsilon_{ij} = \nabla \cdot (u - U)$, where U is the particle displacement of the fluid. μ is the shear modulus and λ_c is the Lamé parameter of the saturated rock. α is defined by $\left(1 - \frac{K_{Dry}}{K_{Solid}} \right)$, where K_{Solid} and K_{Dry} are the bulk moduli of the solid and the dry rock frame. M is the coupling modulus between the fluid and the solid frame and P is the fluid pressure. $V = \frac{\partial u}{\partial t}$ is the solid particle velocity and $W = \frac{\partial}{\partial t} (u - U)$ is the particle velocity of the fluid relative to the solid. The coefficients A to F are the density related coefficients which are defined as: $A = - \left(\frac{\rho_{12} + \rho_{22}}{\rho_{12}^2 - \rho_{11}\rho_{22}} \right)$, $B = \left(\frac{\rho_{11} + \rho_{12}}{\rho_{12}^2 - \rho_{11}\rho_{22}} \right)$, $C = \left(\frac{\rho_{11} + 2\rho_{12} + \rho_{22}}{\rho_{12}^2 - \rho_{11}\rho_{22}} \right)$, $D =$

$$- \left(\frac{\rho_{22}}{\rho_{12}^2 - \rho_{11}\rho_{22}} \right), E = \left(\frac{\rho_{12}}{\rho_{12}^2 - \rho_{11}\rho_{22}} \right), F = -bA, \text{ and}$$

$$\rho_{11} = (1 - \phi) \rho_s + \rho_a, \quad (5)$$

$$\rho_{22} = \phi \rho_f + \rho_a \quad (6)$$

where ρ_f and ρ_s are the fluid and the solid densities, and ρ_a is an additional density caused by the presence of the fluid. ϕ is the porosity and b is the fluid mobility defined by η/κ , where κ and η are permeability and fluid viscosity.

In the 2D case, equations (1) to (4) make a set of 8 coupled equations that could be used for numerical modelling. A finite-difference program was developed in the previous work (Moradi and Lawton, 2013) to simulate wave propagation in isotropic poroelastic media; however, the boundary conditions for the algorithm were not developed at the time. Therefore, to eliminate the artifacts caused by the computational boundaries, a PML condition is added to the program.

Perfectly matched layers

To derive the equations for PML, the regular coordinate variables in the frequency domain are replaced by the complex stretched variables which are defined as:

$$\tilde{x} = \int_0^{x_i} S_i(x_i) dx_i, \quad S_i(x_i) = 1 - a_i/i\omega \quad i = 1, 2, 3 \quad (7)$$

(Chew and Liu, 1996; Sheen et al., 2006), where a_i is the damping factor in x_i direction, and ω is the temporal frequency. Here we show the process of deriving the PML equations for one of the differential equations of motion, and the rest could be derived similarly. Assuming the 2D case where the wave is traveling within the $x - z$ plane, for the vertical particle velocity of the fluid we have:

$$\frac{\partial V_z}{\partial t} = A \left(\frac{\partial \tau_{xz}}{\partial x} + \frac{\partial \tau_{zz}}{\partial z} \right) + B \frac{\partial S}{\partial z} + C W_z \quad (8)$$

which after transforming to the frequency domain becomes:

$$(-i\omega)\hat{V}_z = A \left(\frac{\partial \hat{\tau}_{xz}}{\partial \tilde{x}} + \frac{\partial \hat{\tau}_{zz}}{\partial \tilde{z}} \right) + B \frac{\partial \hat{S}}{\partial \tilde{z}} + C \hat{W}_z \quad (9)$$

From the definition in equation (7) we can use $\partial/\partial \tilde{x}_i = (\frac{1}{S_i})\partial/\partial x_i$ to replace the complex variable \tilde{x}_i by the regular coordinate variable x_i . For simplicity of the equations, the velocities and the stresses are split into x and z components. For example: $V_i = V_i^x + V_i^z$. Equation (8) after change of variables and splitting becomes:

$$(-i\omega)\hat{V}_z^x = \left(\frac{A}{S_x} \right) \left(\frac{\partial \hat{\tau}_{xz}}{\partial x} \right) + C \hat{W}_z^x \quad (10)$$

and

$$(-i\omega)\hat{V}_z^z = \left(\frac{A}{S_z}\right) \left(\frac{\partial\hat{\tau}_{zz}}{\partial z}\right) + \left(\frac{B}{S_z}\right) \frac{\partial\hat{S}}{\partial z} + C\hat{W}_z^z \quad (11)$$

By transforming these equations back to the time domain we have:

$$\left(\frac{\partial}{\partial t} + a_x\right) V_z^x = A \left(\frac{\partial\tau_{xz}}{\partial x}\right) + C \left(W_z^x + a_x \int_{-\infty}^t W_z^x dt\right) \quad (12)$$

$$\left(\frac{\partial}{\partial t} + a_z\right) V_z^z = A \left(\frac{\partial\tau_{zz}}{\partial z}\right) + B \frac{\partial S}{\partial z} + C \left(W_z^z + a_z \int_{-\infty}^t W_z^z dt\right) \quad (13)$$

The same approach could be used to obtain the rest of equations. As previously mentioned, in the 2D case there are 8 coupled equations to solve. The number of equations is doubled after splitting the velocities and stresses in two directions of x and z . This set of 16 equations is approximated using the finite-difference method to simulate the wave propagation in poroelastic media.

The grid is divided into two regions: the internal region and the PML region. The values of a_x and a_z are both zero in the internal grid. In the PML region, these values could be either zero or none-zero depending on the location of the grid point. This is shown in Figure 1. At the corners of the grid, both a_x and a_z are none-zero to help in damping the strong reflections generated in these areas. In our study, a_x and a_z are calculated based on the criteria suggested by Collino and Tsogka (2001). For example:

$$a_x = \log\left(\frac{1}{R}\right) \left(\frac{3V_p}{2}\right) \left(\frac{x^2}{L_{PML}^3}\right) \quad (14)$$

where R is the theoretical reflection coefficient and x is the distance from the PML boundary. $L_{PML} = n_{PML} \times dx$ is the thickness of the PML region, where n_{PML} is the number of the grid points included in the PML boundary, and dx is the grid spacing.

NUMERICAL MODELLING

Finite-difference approximation

As explained earlier, the equations of motion for poroelastic media in the 2D case make a set of 16 equations after applying the PML boundary condition. In order to simulate wave propagation in the poroelastic media, these equations are discretized using a velocity-stress staggered-grid finite-difference approximation. The discretized equations for equations 1 to 4 are presented with more detail in the previous report by the authors (Moradi and Lawton, 2013). Finite-difference approximation could be applied to the PML equations similarly. For example equations 11 and 12 become:

$$V_{z^{i,j+1/2}}^{x^{n+1/2}} = (1 - a_x \Delta t) V_{z^{i,j+1/2}}^{x^{n-1/2}} + \left(A \Delta_x \tau_{xz^{i,j+1/2}}^n + C W_{z^{i,j+1/2}}^{x^{n-1/2}} + C a_x \int_{-\infty}^t W_z^x dt \right) \Delta t \quad (15)$$

$$V_{z^{i,j+1/2}}^{z^{n+1/2}} = (1 - a_z \Delta t) V_{z^{i,j+1/2}}^{z^{n-1/2}} + \left(A \Delta_z T_{z^{i,j+1/2}}^n + B \Delta_z S_{i,j+1/2}^n + C W_{z^{i,j+1/2}}^{z^{n-1/2}} + C a_z \int_{-\infty}^t W_z^z dt \right) \Delta t \quad (16)$$

These equations are used to develop our forward modelling program in Matlab. The algorithm is then tested by numerical models created from the Quest carbon capture and storage project in Alberta.

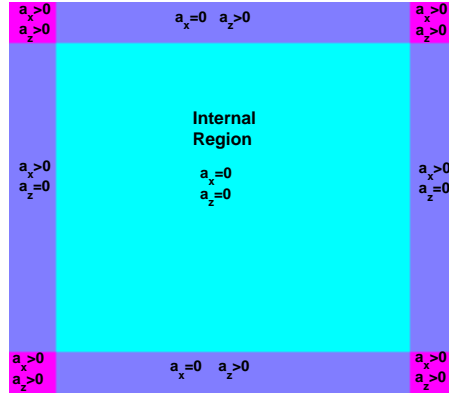


FIG. 1. Schematic view of the PLM region and how the damping factors are defined in two directions.

Single layer model

The numerical model used in this study is based on the Quest CCS project in Alberta. The target formation for injection is the Basal Cambrian Sandstone (BCS) which is a saline aquifer within the Western Canadian Sedimentary Basin (WCSB) (Shell, 2010). In an earlier study (Moradi and Lawton, 2012), the in-situ properties of BCS were extracted from the available well data. These properties are listed in Table 1 as BCS_1 . In addition, using Gassmann’s fluid substitution (Gassmann, 1951; Smith et al., 2003), 40% of the in-situ brine was substituted by CO_2 and the properties of the new saturated BCS were calculated. These values are listed in Table 1 as BCS_2 , and represent BCS after injecting CO_2 .

Table 1. Physical properties of the BCS

Property	BCS_1	BCS_2
ρ_f	1070 (kg/m^3)	937 (kg/m^3)
ρ	2400 (kg/m^3)	2370 (kg/m^3)
V_p	4100 (m/s)	3800 (m/s)
V_s	2390 (m/s)	2400 (m/s)
ϕ	16%	16%
η	0	0

To examine the PML boundary condition, we define a single layer model with the properties of BCS_1 . A Ricker wavelet with the dominant frequency of 40 Hz is used as an explosive source in the finite-difference algorithm. The temporal and spatial sampling

rates were chosen to be 0.2 ms and 2 meters, respectively. The unknowns are the solid and fluid particle velocities and the stresses that need to be calculated by the program. Figure 2a shows the calculated vertical component of the solid particle velocity for this model at the time of 0.15 s. As expected from the Biot's theory, a slow wave (P_s) is generated due to the relative movement of the fluid with respect to the solid. Without boundary conditions, the outgoing wave generates strong reflections from the boundaries of the model (Figure 2.b). After applying the PML to the algorithm, the artifacts are strongly attenuated. Figure 2c to 2e show the results for the PML with three different thicknesses of 15, 20, and 25 grid points at the time of 0.23 s. There is a significant improvement in absorbing the outgoing wave when increasing the PML from 15 to 20 grid points. However, going to 25 grid points from 20 does not make a considerable change. For this example, 20 grid points seems to be satisfactorily efficient. Regardless of the PML thickness, there are still some reflection from the boundaries which could not be completely removed.

A point worth considering is that having a sharp transition from the internal grid to the PML grid could also generate some reflections. This problem could be partially resolved by smoothing the damping factors a_x and a_z . Figure 3 shows the same example for $n_{PML} = 20$ both before and after smoothing the damping factors. The smoothed PML seems to absorb the outgoing wave more effectively than the original PML. Figure 4 shows seismic traces generated based on this model, and the smoothed PML boundaries are compared with the none-smoothed ones for two cases of $n_{PML} = 15$ and $n_{PML} = 20$. It is obvious that in both cases, smoothing the damping factors reduces the reflected waves from the computational boundary considerably.

Two layer model

A second model is generated based on the properties listed in Table 1. This model consists of two layers: BCS_1 , on the top, and BCS_2 at the base. As explained previously, BCS_1 represents the BCS properties before injecting any CO_2 . The rock properties of BCS after injecting CO_2 is represented by BCS_2 . These layers are in fact two sandstones with the same solid properties but different fluid content. The change in the fluid content of the rock leads to a change in the seismic response of the model. Figure 5a shows a snapshot from the vertical particle velocity of the solid calculated for this model. As expected from the Biot's theory, a slow P-wave (P_s) is generated due to the fluid movement. There are also some wave conversions at the boundary. For example: slow P-wave converted to a fast P-wave ($P_s P_f$), and fast P-wave converted to a slow P-wave ($P_f P_s$). To compare our algorithm with an elastic one, the fluid properties are set equal to zero to perform elastic modelling. Figure 5b shows the elastic snapshot. This figure illustrates how these algorithms simulate the wave propagation differently. However, in the seismic frequencies the slow P-wave could not be recorded, since it is diffusive, but the energy loss caused by this wave changes the wave-field.

Time-lapse modelling

Poroelastic modelling could be useful in projects where the pore fluid changes through time, including CCS projects. The main goal of this work is to use the poroelastic algorithm

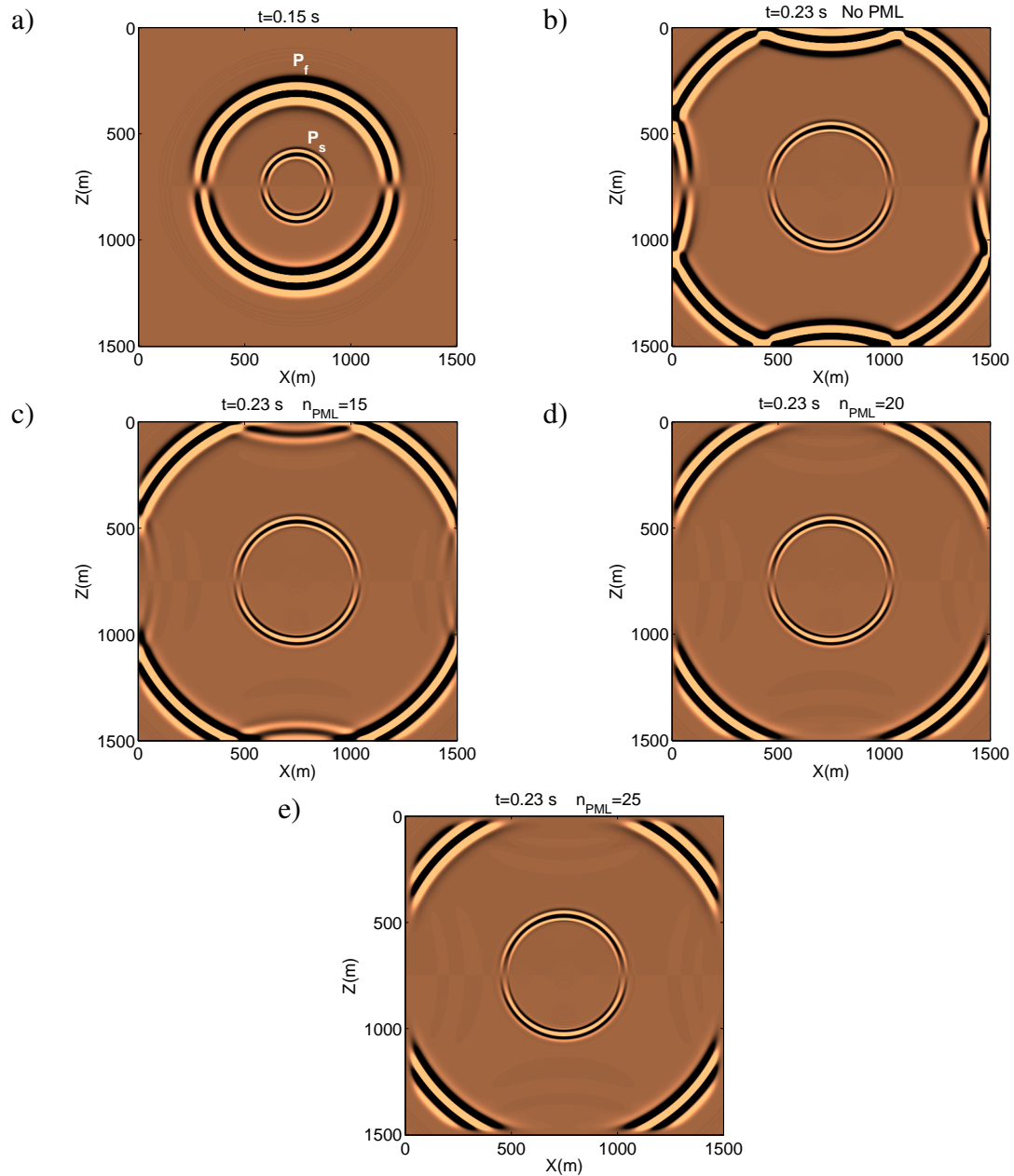


FIG. 2. Snapshots of the vertical particle velocity of the solid at time 0.15 seconds(a) and 0.23 seconds (b) to(e) with different values of n_{PML} : b) zero, c)15, d) 20, and e) 25 grid points

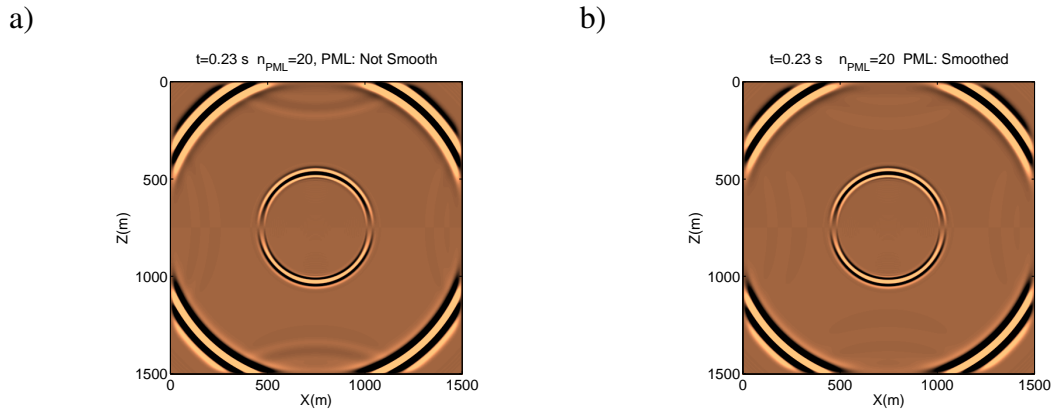


FIG. 3. Same snapshots from Figure 2.d, with a not smoothed PML (a) and a smoothed PML (b).

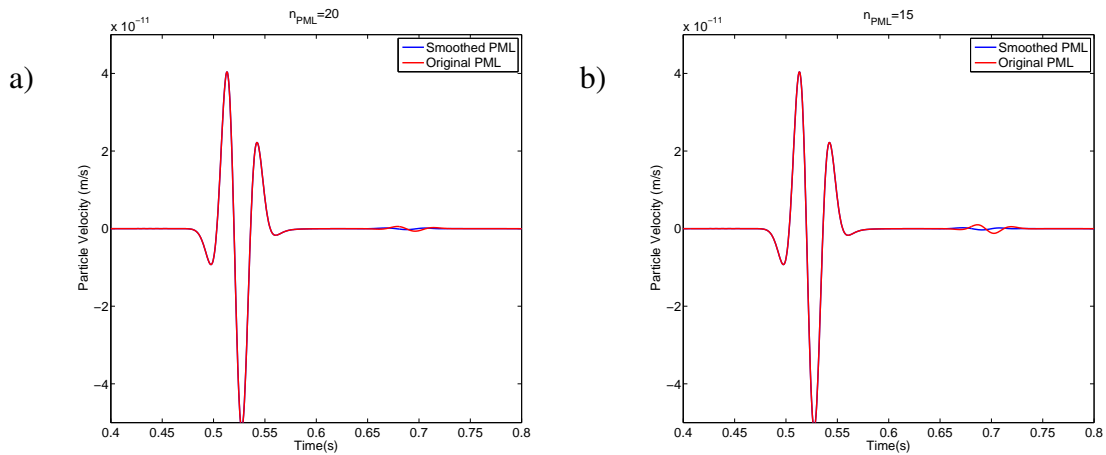


FIG. 4. Traces from the example in Figure 2 with 20 grid points PML (a), and 15 grid points PML (b). The results with the smoothed PML is the curve in blue, and the one without smoothing is the curve in red.

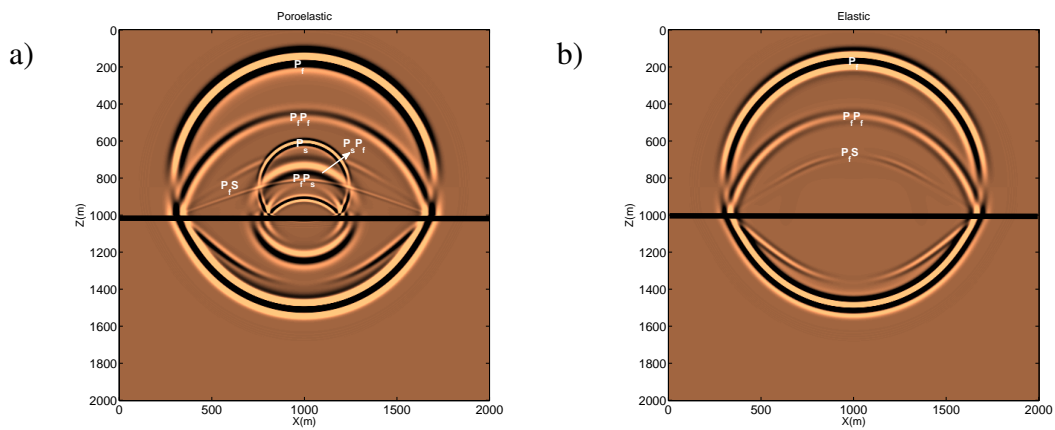


FIG. 5. Snapshots of the vertical particle velocity of the solid for the two layer model at time 0.24 seconds: (a) Poroeelastic modelling; (b) elastic modelling. The horizontal line at the depth of 1000m represents the boundary.

for a CCS project to perform theoretical detectability analysis of the CO_2 . For this purpose a coarse model is made based on the log data from the Quest project. This model that is shown in Figure 6a consists of four main layers. We assume that all layers except BCS are elastic. BCS is located between the depths of 2000 and 2050 meters and could not be distinguished from the upper layer due to the low contrast in the velocity of the two layers. This model is used as our baseline model where the properties of BCS are the same as BCS_1 in Table 1. For the monitor scenario a CO_2 plume is added to the baseline model to simulate a subsurface model after injecting CO_2 . The properties of the plume are the same as BCS_2 in Table 1 which represents the BCS with 40% CO_2 saturation. The size of the plume is calculated based on the amount of injected CO_2 in one year that is 1.2 million tonnes. Assuming the porosity of 16% for the BCS, and 40% CO_2 saturation, the volume of the plume will be $3 \times 10^7 m^3$. If we consider a cylinder as the CO_2 plume, the radius of the plume will be 800 m and its height will be 50 meters which is the thickness of BCS. In our 2D model, the plume appears as a $800m \times 50m$ block (Figure 6b).

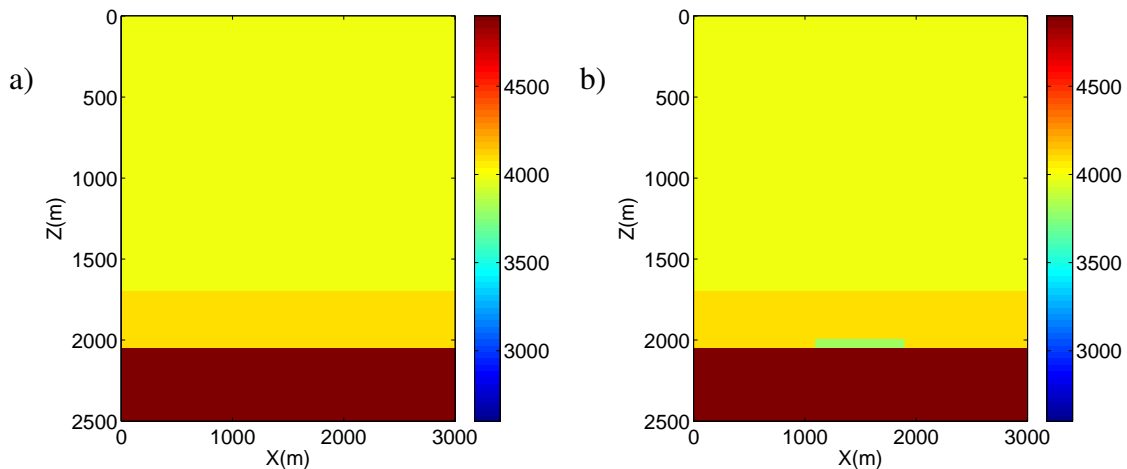


FIG. 6. a) Baseline and b) monitor model generated based on the Quest project. The color-bar shows the p-wave velocity of the saturated rock in m/s.

Both models are then used to generate shot gathers. The grid spacing and temporal spacing are 4 m and 0.2 ms, and the PML boundary has 20 grid points. Figure 7 shows sample shot gathers from the vertical component of the solid particle velocities for both baseline and monitor scenarios. These shot gathers are then used to generate the zero offset sections shown in Figure 8. Injecting CO_2 into BCS causes a change in the properties of the saturated rock. These changes lead to a shift in travel-times for the waves traveling through the plume and a change in the reflection from the top and the base of the plume. The time-lapse effect could be observed by subtracting the monitor section from the baseline section. Figure 9a shows the residual section after subtraction. This section needs to be migrated since there are some diffractions from the edges of the CO_2 plume. An elastic Kirchhoff migration algorithm was used to migrate this section. The result is shown in Figure 9b. The effect of the plume is clearly visible in this section. Selected traces from the modeled monitor and the baseline sections are shown in Figure 10. The amplitude of the reflections from the top and the base of the BCS have increased in the monitor scenario due to CO_2 injection. There is also a time shift for the reflection from the base of the plume since

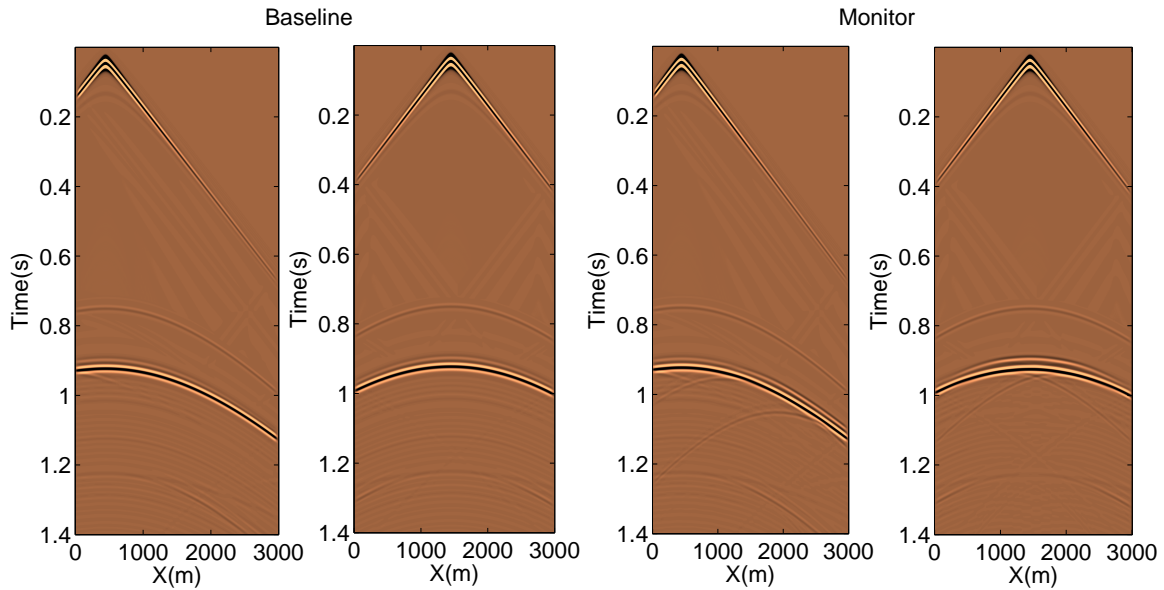


FIG. 7. Sample shot gathers generated for baseline (two shots in the left) and monitor (two shots in the right) scenarios using the poroelastic finite-difference algorithm.

the wave is traveling through a slower layer after injecting CO_2 . The difference between the baseline and the monitor traces (the solid black curve) shows that the amplitude of the residual trace is comparable with the amplitude of the signal. This means that the CO_2 plume could be detected in the seismic data providing the data have good bandwidth and a high signal to noise ratio. The dashed brown curve shows the difference between the time-lapse effect in the poroelastic algorithm and the one in the elastic algorithm. This difference is about 10% of the maximum amplitude of the baseline (or monitor) trace. In addition, the thickness of our target layer was only 50 meters which makes the difference between the two algorithms small. Any other property that effects the fluid flow could also effects the difference between the elastic and the poroelastic algorithms. For example, the porosity of the rock or any of the fluid properties might change the calculated wave-field. Therefore, our program needs to be examined for different models to understand the changes that these properties cause on the wave-field.

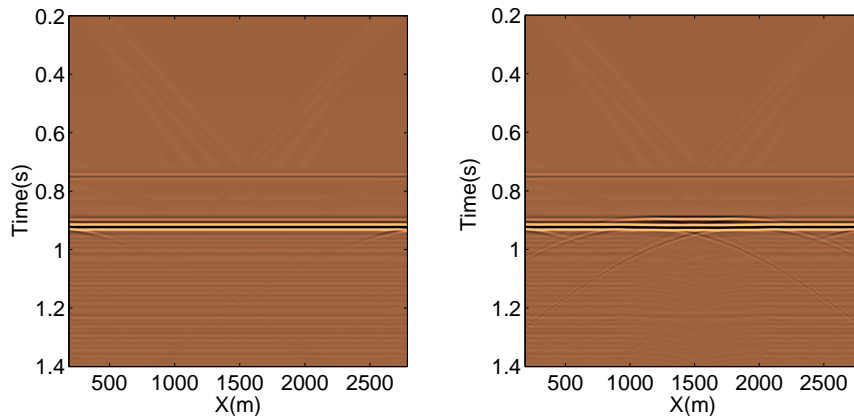


FIG. 8. Calculated zero offset sections for the baseline (a) and the monitor (b) scenarios.

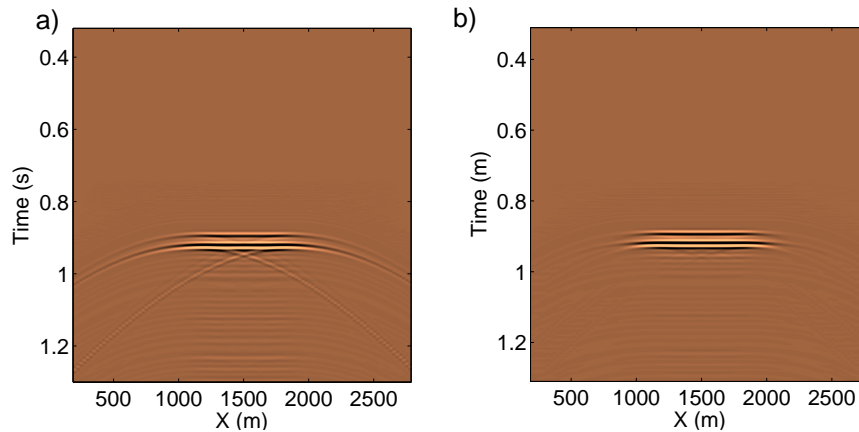


FIG. 9. Time-lapse difference between the two zero offset sections in figure 8 before (a) and after (b) Kirchhoff time migration.

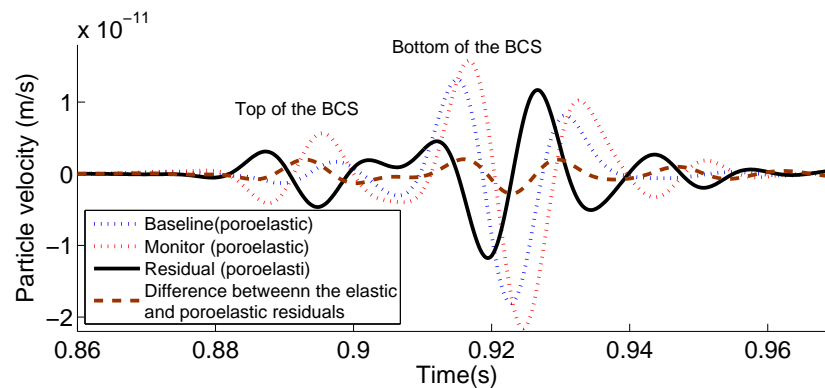


FIG. 10. Selected traces from the zero offset sections in figure 8. The solid black curve shows the time-lapse residual and the dotted brown curve shows the difference between the residuals calculated by elastic and poroelastic algorithms.

CONCLUSION

Model based poroelastic time-lapse modelling was performed for the Quest carbon capture and storage project in Alberta. A finite-difference code was developed in Matlab based on the Biot's theory of poroelasticity in which the properties of the pore fluid are taken into account in wave propagation. Based on the results, the CO_2 plume could be detected in the seismic data after one year of injection if the data is of good quality. However, a comparison between the poroelastic algorithm and a elastic one shows a small difference between the time-lapse residual calculated by those two algorithm. The reason could be the target poroelastic layer being relatively thin. However the the poroelastic algorithm is being examined for different fluid properties as well as layer thicknesses and porosity to investigate the effect of these parameters on the calculated wavefield.

ACKNOWLEDGMENTS

This research has been supported by the CREWES sponsors, Carbon Management Canada (CMC), and Natural Science and Engineering Research Council of Canada (NSERC) through the grant CRDPJ 379744-08. Hassan Khaniani, Peter Manning, Joe Wong, Roy

Lindseth from CREWES, David Aldridge from Sandia National Laboratories, and Juan Santos from Purdue University are acknowledged for their helpful comments and discussions. We also thank Shell Canada Limited for providing the well data.

REFERENCES

- Berenger, J. P., 1994, A perfectly matched layer for absorption of electromagnetic waves: *Journal of Computational Physics*, **114**, 185–200.
- Biot, M. A., 1962, Mechanics of deformation and acoustic propagation in porous media: *Journal of Applied Physics*, **33**, 1482–1498.
- Carcione, J. M., Morency, C., and Santos, J. E., 2010, Computational poroelasticity-a review: *Geophysics*, **75**, No. 5, 75A229–75A243.
- Chew, W., and Liu, Q., 1996, Perfectly matched layers for elastodynamics: a new absorbing boundary condition: *Journal of Computational Acoustics*, **4**, 341–359.
- Collino, F., and Tsogka, C., 2001, Application of the perfectly matched absorbing layer model to the linear elastodynamic problem in anisotropic heterogeneous media: *Geophysics*, **66**, No. 1, 294–307.
- Dai, N., Vafidis, A., and Kanasevich, E., 1995, Wave propagation in heterogeneous, porous media:a velocity-stress, finite-difference method: *Geophysics*, **60**, 327–340.
- Gassmann, F., 1951, Über die elastizität poroser medien: *Vierteljahresschrift der Naturforschenden Gesellschaft in Zurich*, **96**, 1–23.
- Gurevich, B., Zyrianov, V. B., and Lopatnikov, S. L., 1997, Seismic attenuation in finely layered porous rocks: effects of fluid flow and scattering: *Geophysics*, **62**, No. 1, 319–324.
- Moradi, S., and Lawton, D. C., 2012, Time lapse seismic monitoring of co2 sequestration at quest ccs project: CREWES Research Report, **24**.
- Moradi, S., and Lawton, D. C., 2013, Velocity-stress finite-difference modeling of poroelastic wave propagation, Tech. rep.
- Shapiro, S. A., and Müller, T. M., 1999, Seismic signatures of permeability in heterogeneous porous media: Short note: *Geophysics*, **64**, No. 1, 99–103.
- Sheen, D. H., Tuncay, K., Baag, C., and Ortoleva, P., 2006, Parallel implementation of a velocity-stress staggered-grid finite-difference method for 2-d poroelastic wave propagation: *Computers and Geosciences*, **32**, 1182–1191.
- Shell, 2010, Quest carbon capture and storage project: Project description, **1**.
- Smith, T., Sondergeld, C., and Rai, C. S., 2003, Gassmann fluid substitutions: A tutorial: *Geophysics*, **68**, No. 2, 430–440.